Direct measurements of colloidal friction coefficients

Stuart Henderson, Steven Mitchell, and Paul Bartlett*
School of Chemistry, University of Bristol, Bristol BS8 1TS, United Kingdom
(Received 8 May 2001; revised manuscript received 13 August 2001; published 26 November 2001)

The time-independent hydrodynamic forces operating between two hard spheres were studied as a function of the interparticle separation r. Two colloids were positioned a distance r apart using a dual-beam optical tweezer similar to that described by Meiners and Quake [Phys. Rev. Lett. **82**, 2211 (1999)]. Brownian fluctuations in the positions of the two spheres were followed by recording the intensity of forward scattered laser light. The two particles move cooperatively as a result of hydrodynamic forces. The strength of the correlation increased strongly with decreasing separation r. We show that the temporal and spatial correlations in the particle displacements are determined by the distance dependence of the pair friction tensor ξ. The distance and geometry dependence of the measured friction tensor is found to be in excellent agreement with the predictions of low-Reynolds number calculations.

DOI: 10.1103/PhysRevE.64.061403 PACS number(s): 82.70.Dd, 47.15.Gf, 05.40.−a

I. INTRODUCTION

Hydrodynamic interactions play a crucial role in determining the dynamical properties of colloidal suspensions [1]. For instance, the rheological behavior of colloidal systems under shear fields [2], the kinetics of crystallization [1], aggregation, and the structure of long-lived metastable phases such as colloidal gels [3] are all believed to be influenced strongly by many-body hydrodynamic forces. The origin of these forces is classical; each particle, when moving through a viscous fluid, creates a long-range flow disturbance $\delta\mathbf{v}(r)$, which reacts on the motion of other particles, producing a time-dependent interaction between distant particles. While the hydrodynamic forces acting between two spheres at low-Reynolds number was calculated some ninety years ago [4], the hydrodynamic forces in more complex situations, such as the sedimentation of colloidal particles [5], or within concentrated suspensions [6], still remains controversial. A serious obstacle to an improved understanding of these situations is the long-ranged nature of hydrodynamic interactions, which decays as $1/r$. Consequently, perturbative solutions are generally invalid and hydrodynamic interactions in many situations are truly many-body properties. Recently, there has been a renewed *experimental* interest in the direct measurement of hydrodynamics in ''simple'' colloidal systems [7–11]. This interest has stemmed from the development of a single-particle trapping technique that allow the manipulation and measurement of individual particles with an accuracy approaching a few nanometers. These techniques offer the possibility of quantitatively testing hydrodynamic theories. In this paper, we use single-particle techniques to make a detailed measurement of the functional form of the time-independent hydrodynamic interactions between an isolated pair of colloidal spheres. Our measurements probe the distance dependence of the hydrodynamic interactions and span both the asymptotic far-field region where hydrodynamic forces decay as $1/r$ and the near-field region where lubrication forces become significant.

We study the simplest interacting Brownian system, which consists of two spherical particles of radius a separated by a distance r in an infinite, incompressible fluid of viscosity η at a temperature T. When the separation between the two spheres is large in comparison with the interparticle potential, the two spheres are coupled only via hydrodynamic forces. A random solvent collision with either of the two spheres sets the surrounding fluid into motion. The momentum transferred to the fluid spreads throughout the system at a rate controlled by the sound velocity and the kinematic shear viscosity ν of the fluid. When the rapidly propagating flow field arrives at the surface of a second sphere, the velocity field is modified as a result of the boundary conditions at the particle surface and a time-dependent force is generated that couples the motions of both spheres together. Colloidal particles are so sufficiently large in comparison to fluid molecules that there is a large separation in time scales between the small but finite time taken for the hydrodynamic fields to propagate between the two particles (typically $\sim 10^{-7}$ s) and the subsequent diffusion of the particles ($\sim 10^{-4}$ s). Consequently, there is a substantial period over which the hydrodynamic flow fields $\delta\mathbf{v}(r)$ are essentially time independent, before the Brownian particles have noticeably moved. It is the resulting *quasistatic* hydrodynamic interactions that are the subject of this paper.

This paper describes a detailed experimental investigation of the quasistatic hydrodynamic coupling between two isolated colloidal spheres. We use single-particle manipulations and laser deflection techniques, similar to those described in Ref. [8], to measure directly each of the four distinct components of the friction tensor as a function of the pair center-to-center separation r. We make a detailed comparison between our experiments and available theoretical predictions. Our paper is organized as follows: In the next section, we describe the details of our experiment. In Sec. III, we summarize the Brownian motion of a pair of hydrodynamically coupled spheres. We present our results in Sec. IV before concluding.

*Electronic address: P.Bartlett@bristol.ac.uk

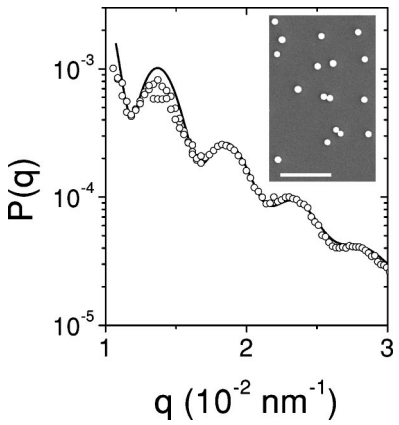

FIG. 1. The circles depict the measured form factor $P(q)$ as a function of the scattering wave-vector q for the colloidal spheres used in this paper. The curve shows the scattering calculated for a dilute suspension of homogeneous spheres of mean radius $a=652$ nm, and polydispersity $p=6\%$. The inset shows a SEM micrograph of the spheres. The scale bar is 10 μm long.

II. MATERIALS AND METHODS

A. Synthesis and characterization

The colloidal suspension used consists of fluorescently labeled poly(methyl methacrylate) [PMMA] spheres dispersed in a mixture of cyclohexane and *cis*-decalin. The particles were prepared following the procedures described in Ref. [12], by a free-radical dispersion polymerization of a mixture of methyl methacrylate (54% by mass), hexane (30% by mass) and dodecane (16% by mass) using a poly(methyl methacrylate)-poly(12-hydroxy stearic acid) [PMMA-PHSA] comb copolymer as stabilizer. The fluorescent agent, Nile Red, was incorporated into the reaction mixture in order to fluorescently tag the particles. The particles contained a final dye concentration estimated at $71\mu M$ and are sterically stabilized by a physically adsorbed polymeric brush (estimated to be $\sim$10 nm thick). The PMMA-PHSA stabilizer layer was subsequently covalently locked to the surface of the particles by a high-temperature esterification. The fluorescent spheres were separated from the reaction mixture, cleaned by centrifugation, and redispersed in a mixture of cyclohexane and *cis*-decalin. Previous studies [1] have shown that the potential between PMMA-PHSA stabilized spheres suspended in a hydrocarbon is essentially hard spherelike with a strong short-range repulsion and negligible attraction.

The synthesized particles were characterized by a combination of electron microscopy and light scattering. Scanning electron microscopy (SEM) images were collected using a JEOL JSM-6310 microscope. From an analysis of the SEM micrographs (inset in Fig. 1) the standard deviation of particle radii, $p=\sqrt{\langle a^2\rangle-\langle a\rangle^2}/\langle a\rangle$, was determined as 4%. The value for the number-averaged radius $\langle a\rangle$ from SEM was found to be unreliable because of electron-beam damage so an accurate value for $\langle a\rangle$ was determined from static light scattering (SLS) measurements. The time-averaged scattering from a very dilute suspension of the particles in *cis*-decalin was measured at $\lambda=488$ nm using a Malvern 4700 spectrometer. A 488 nm laser-line interference filter was placed in front of the photomultiplier to separate the scattered intensity from fluorescence emission. To minimize distortions from multiple scattering, measurements were taken over a range of dilutions starting from a volume fraction $\phi\approx1\%$ and decreasing until the dilution-corrected intensity remained unchanged. Figure 1 depicts the measured particle form factor $P(q)$ and a theoretical curve calculated for a homogeneous sphere of mean radius $\langle a\rangle=652$ nm and a polydispersity p of 6%. The discrepancies seen at low-scattering vector are probably a consequence of back reflections or core-shell interference effects.

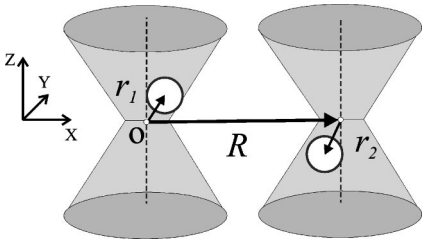

FIG. 2. Schematic diagram of dual-beam optical tweezer. The foci of the two orthogonally polarized beams are located at the origin O and at the end of the vector **R**. Axes are used with the x axis parallel to the vector **R** and the y axis lying in the focal plane of the two beams. Vectors $\mathbf{r}_1$ and $\mathbf{r}_2$ define the positions of the two Brownian spheres. The particle center-to-center separation vector is $\mathbf{r}=\mathbf{r}_2-\mathbf{r}_1+\mathbf{R}$.

B. Dual-beam optical tweezers

The details of the dual-beam optical tweezer equipment used have been described elsewhere [13]. A schematic of the apparatus is shown in Fig. 2. In brief, our apparatus is built around a modified inverted microscope (Axiovert S100 with optics from Carl Zeiss) mounted on a vibration-isolated optical table. Two optical traps were created by tightly focusing orthogonally polarized beams from a near-infrared laser ($\lambda=1064$ nm, Nd-YAG, maximum power 0.5 W cw, 7910-Y4-106, Spectra-Physics) using an oil immersion objective ($100\times/1.3$ NA, Plan Neofluar, Zeiss). The optical gradient forces are strong enough to localize the spheres near the foci of the two beams so that the center-to-center separation of the two particles could be systematically varied by moving the two beams. For small displacements of the particles from the optical axis of each trap the optical gradient forces are harmonic. The external restoring force on a sphere F_{ext} is then simply proportional to its (lateral) displacement $F_{ext}=-k(x+y)$ where the coordinates x and y lie within the focal plane. The force-constant k is a function of the size and optical properties of the trapped sphere.

The thermal motion of the trapped spheres was measured by recording the interference between the forward scattered light and the transmitted laser beam in the back-focal plane of the microscope objective [14] using two quadrant photodetectors, one for each polarized beam. Displacement of a refractive sphere away from the optical axis causes the far-field angular-interference pattern to become noncircular. For small displacements, compared to the radius of the waist of

the focused beam, the deviation from circularity is linear in the particle displacement. The fluctuating change in the interference pattern at the quadrant detector is recorded along two perpendicular directions by calculating the difference between the sum of the horizontal and vertical quadrant signals using custom-built low-noise current-to-voltage converters. The analog signal is amplified, filtered, and then digitized using a 12-bit A/D card (PCI-MIO-16E-4, National Instruments) with data acquisition software written in Labview (National Instruments).

The samples studied consisted of a 170 μm thick layer of a very dilute suspension of PMMA spheres ($\phi = 5 \times 10^{-6}$). The suspension was contained within a custom-made rectangular capillary cell with walls 170 μm thick (close to the thickness of standard #1 coverslips), so that optical distortions were minimized. The cell was completely filled, before the ends of the capillary cell were hermetically sealed with a rapid setting epoxy resin. The colloidal spheres (with a refractive index n_c of 1.494) were suspended in a mixture of cyclohexane (72.1%, by weight) and *cis*-decalin with an overall refractive index (n_s) of 1.431 and viscosity $\eta = 1.22$ mPa s. The composition of the solvent mixture was determined by a compromise between the need to generate a large and positive refractive index mismatch between colloid and solvent to maximize trapping forces and a desire to minimize the refractive index difference between suspension and immersion oil ($n_{oil} = 1.518$) to reduce spherical aberation. Increased spherical aberation reduces the depth inside the cell at which spheres may be trapped and so increases the likelihood of significant hydrodynamic coupling of the particles to the walls of the cell. The composition chosen allowed reasonably strong trapping forces to be generated deep within the cell and at least 40 μm from cell walls. Finally, to eliminate adsorption of colloidal spheres onto the walls of the cell a low concentration of the PMMA-PHSA stabilizer was added to the suspension. The free stabilizer absorbs strongly onto the glass walls of the cell generating thick polymeric layers so that particles could be readily removed using optical forces. The sample chamber was glued to a microscope slide for ease of handling and mounted on a piezoelectric translation stage for fast and accurate position and motion control.

C. Calibration

Calibration of the instrument was carried out in two stages. First, the detector response was determined by scanning an immobilized particle through a stationary laser trap and recording the resulting signal. A capillary cell with a colloidal particle adsorbed onto its lower surface was mounted on a piezoelectric translation stage (Physike Instrumente P-517 2CL) and driven with a sine wave of amplitude 1 μm at a frequency of 0.1 Hz. Capacitative position sensors (Physike Instrumente E-501.00) were used to monitor the position of the stage and correct for the nonlinearity and hysteresis of the piezoactuators. The detector response was recorded for about 1000 s and analyzed by plotting the detector voltage against particle position. The slope of the linear central region of this plot was estimated by linear regression from an averaged response-displacement curve. The resulting sensitivity factor was used to convert the detector voltage signals into particle displacements. The procedure was repeated for motion along the second orthogonal axis. We found that the measured sensitivity varied significantly with the axial position of the particle even in the range of ± 0.5 μm where the particle appeared to be focused in the image. Because of the resulting problems of reproducibility, we adopted routinely an alternative more robust procedure to calibrate the detectors that had the advantage of yielding rapid simultaneous estimates of both the sensitivities and stiffness of the optical trap.

The method depended on a measurement of the thermally driven position fluctuations of a single trapped particle. The mean-squared displacement $\langle \Delta x^2(t) \rangle$ of a Brownian sphere in a harmonic potential has been analyzed in detail by Uhlenbeck and Ornstein [15]. Their analysis reveals that for times long compared with the relaxation time of the velocity autocorrelation function, $\langle \Delta x^2(t) \rangle$ increases exponentially with time,

$$\langle \Delta x^2(t) \rangle = \langle \Delta x^2 \rangle_\infty \left[1 - \exp\left(- \frac{2 D_0 t}{\langle \Delta x^2 \rangle_\infty} \right) \right], \tag{1}$$

with D_0 the free-diffusion constant, which for an isolated particle, is given by the Stokes-Einstein expression $D_0 = k_B T / 6 \pi \eta a$. The detector voltage $V(t)$ is proportional to the particle displacement $V(t) = C x(t)$, so the time-averaged mean-squared detector is similarly

$$\langle \Delta V^2(t) \rangle = \alpha (1 - e^{-\beta t}). \tag{2}$$

The constants α and β are functions of the detector sensitivity C and trap stiffness k. Inverting this relationship gives expressions for the two calibration constants, C and k, in terms of measurable quantities,

$$C = \sqrt{\alpha \beta / (2 D_0)},$$

$$k = \beta k_B T / D_0. \tag{3}$$

To calibrate the detector, the voltage record from a single trapped PMMA particle, far away from either the walls of the capillary or other particles, was measured for at least 52 s (2^{20} data points). The mean-squared fluctuation in the detector signal $\langle \Delta V^2(t) \rangle$ was calculated and fitted by a nonlinear least squares algorithm to Eq. (2). The detector sensitivity and trap stiffness were found from Eq. (3), using measured values for the solvent viscosity and particle radius. This procedure was very reproducible with the scatter in the sensitivities and force constants for individual particles being about $\pm 3\%$ (coefficient of variation). However, we found significantly larger variations ($\pm 10\%$) when a number of different particles were used. We ascribe this variation to the small but finite polydispersity of our particles.

D. Cross correlations

The Brownian fluctuations in position of an individual pair of spheres were measured. Two spheres were trapped in

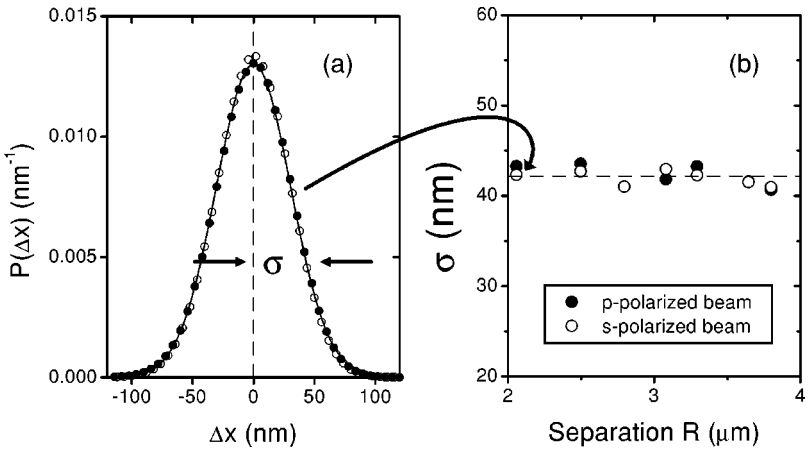

FIG. 3. Measurement of the single-particle distribution function $P(\Delta x)$ for displacements Δx parallel to the center-to-center vector **R**. Part (a) shows a typical histogram, measured with spheres trapped in both the *p*- (filled circles) and *s*-polarized traps (open circles) at a trap separation of $R=2.06\ \mu$m. Fitting to a Gaussian yields the rms displacement σ. The measured values of σ (b) do not change with the laser-trap separation *R*, confirming that the two optical traps are independent of each other.

the same focal plane, 40 μm above the lower glass wall and 130 μm from the upper wall. All other particles in the field of view were removed. The instantaneous positions of the two spheres were collected and digitized at 20 kHz. To prevent aliasing of high-frequency noise from the amplifier electronics, signals were passed through a low-pass filter with a bandwidth of 34 kHz before digitizing. Particle trajectories were recorded for 419 s (2^{23} data points) to ensure adequate statistical averaging. Immediately after recording the thermal fluctuations of a particle pair and before moving to the next pair separation, each of the laser beams was blocked in turn and the stiffness and sensitivity of both traps were determined by the methods outlined in Sec. II C. To minimize scatter in single-particle experiments, it is important to use the same individual pair of particles. To do this, one of the spheres was first deposited at the bottom of the cell before the appropriate beam was turned off. The Brownian motion of the remaining sphere was then recorded for 52 s (2^{20} data points) before, in turn, this particle was stored at the base of the cell and the second beam was calibrated. After calibration, both lasers were then turned on, the same two particles trapped, and the trap separation reduced. Particle fluctuations were measured at a total of twelve different pair-separations *r* ranging from 2.06 to 18.87 μm using two different individual sets of particles. The spacing between the centers of the two traps was measured with an accuracy of about 40 nm by identifying the centers of trapped spheres using a centroid tracking algorithm.

The data were analyzed using a suite of routines, implemented using the IDL programming language (Research Systems). The analysis was complicated by the pointing instability of our laser. The instability caused the positions of the laser traps to move apparently randomly within the focal plane over distances of order 10 nm on a time scale of a few seconds. These small and slow variations have no significant effects on the dynamics of the trapped spheres that track the laser beam rapidly. However, they complicate the extraction of trajectory information from the voltage record $V(t)$. To reduce the resulting drifts in the baseline, all experimental data was split into short blocks typically containing 2^{14} data points (0.8 s). Each block was analyzed separately before the individual results were averaged together. By this means, fluctuations in the data that decay on times long compared with the block interval are suppressed, while the rapid fluctuations, which constitute the signal of interest, are not attenuated.

Before determining the dynamical two-particle correlations, the equilibrium single-particle distributions was first checked. The probability of finding a one-dimensional displacement Δx from the trap origin is Gaussian,

$$P(\Delta x)=\frac{1}{\sqrt{2\pi\sigma^2}}e^{-(\Delta x^2/2\sigma^2)}, \tag{4}$$

with σ the root-mean squared (rms) displacement $\langle x^2\rangle^{1/2}$. At each pair separation, the distribution functions were calculated for motions parallel and perpendicular to **R**. A selection of normalized distributions are depicted in Fig. 3(a) where it is clear that the experimental distributions are accurately represented by Gaussians. The rms width σ does not change with trap separation [Fig. 3(b)]. Consequently, there are no measurable interparticle forces acting between the particles at separations $>2\ \mu$m.

To study the dynamical correlations between the trapped spheres, the normalized functions,

$$h_{ij}(t)=\frac{\langle x_i(t)x_j(0)\rangle}{\sqrt{\langle x_i^2\rangle\langle x_j^2\rangle}},$$

$$g_{ij}(t)=\frac{\langle y_i(t)y_j(0)\rangle}{\sqrt{\langle y_i^2\rangle\langle y_j^2\rangle}} \tag{5}$$

(with subscripts *i* and *j* labeling the traps) were determined from the particle trajectories using a fast fourier transform (FFT) algorithm. A coordinate system was chosen (with laser traps at position vectors $\mathbf{R}_1$ and $\mathbf{R}_2$) so that the *x* axis is orientated along the vector, $\mathbf{R}=\mathbf{R}_2-\mathbf{R}_1$ connecting the two laser traps, the *z* axis is parallel to the laser beam, and the origin at the focus of beam one (Fig. 2).

The cross-correlation functions measured were corrected for the effects of depolarization (less than a few percent) which occurs as a polarized beam passes through a high-NA microscope objective. Any depolarization of the *s*-polarized beam generates, for instance, a weak *p*-polarized signal,

which is recorded by the p detector. Accordingly, there is an instantaneous contribution form depolarization to the measured cross correlations. To remove this artifact, the cross correlation of the outputs of the s and p detectors was measured with each of the two laser beams alternately turned off. Combining measurements of the cross-correlation function when both lasers are on $[C_{sp}(t)]$, and with just one laser on [either the s laser $C_s(t)$, or the p laser $C_p(t)$] provided an estimate of the sample cross correlation $C(t)$ as

$$C(t)=C_{sp}(t)-C_s(t)-C_p(t). \tag{6}$$

The depolarized correction functions $C_s(t)$ and $C_p(t)$ did not vary with particle separation and they were therefore determined from the calibration runs.

III. THEORETICAL ANALYSIS

For completeness, we summarize here the stochastic motion of a pair of Brownian particles correlated only by hydrodynamic forces. We consider two spherical particles, each of mass m and radius a, immersed in an unbounded incompressible fluid of shear viscosity η and confined by the external potential,

$$V_{ext}(\mathbf{r}_1,\mathbf{r}_2)=\frac{1}{2}k\mathbf{r}_1^2+\frac{1}{2}k\mathbf{r}_2^2. \tag{7}$$

When a sphere is set into motion by a thermal fluctuation, it sets the surrounding fluid into motion. The resulting hydrodynamic force is transmitted to a particle a distance r away on a time of order $\tau_v=r^2/\nu$. On times $t\gg\tau_v$, hydrodynamic interactions reach their long-time asymptotic or Stokes limit. Since the time scale of our experiments ($t\sim10^{-3}$ s) is much larger than τ_v, we may safely ignore propagation effects. In the quasistatic limit, hydrodynamics are described by the linear Navier-Stokes equations for steady, incompressible flow [16]. The linearity of these equations ensures that the hydrodynamic force $-\mathbf{F}_i$ exerted by the fluid on the ith sphere is a linear function of the translational velocities $\mathbf{u}_i$,

$$\begin{pmatrix}\mathbf{F}_1\\ \mathbf{F}_2\end{pmatrix}=\begin{pmatrix}\boldsymbol{\xi}_{11} & \boldsymbol{\xi}_{12}\\ \boldsymbol{\xi}_{12} & \boldsymbol{\xi}_{11}\end{pmatrix}\begin{pmatrix}\mathbf{u}_1\\ \mathbf{u}_2\end{pmatrix}, \tag{8}$$

with the friction tensors $\boldsymbol{\xi}_{ij}$ as coefficients. A system of two spheres is axially symmetric about its line of centers, $\mathbf{r}=\mathbf{r}_2-\mathbf{r}_1$, and so the friction tensor may be split into elements parallel, $\boldsymbol{\xi}_{ij}^{\parallel}$, and perpendicular to $\mathbf{r}$, $\boldsymbol{\xi}_{ij}^{\perp}$,

$$\boldsymbol{\xi}_{ij}=\boldsymbol{\xi}_{ij}^{\parallel}\frac{\mathbf{rr}}{r^2}+\boldsymbol{\xi}_{ij}^{\perp}\left(\mathbf{1}-\frac{\mathbf{rr}}{r^2}\right). \tag{9}$$

In consequence, only four coefficients ($\xi_{11}^{\parallel}$, $\xi_{12}^{\parallel}$, $\xi_{11}^{\perp}$, and $\xi_{12}^{\perp}$) are needed to fully quantify the hydrodynamic forces between two spheres.

The Langevin equation for a system of two harmonically bound spheres is

$$\begin{aligned} m\frac{d\mathbf{u}_1(t)}{dt}&=-\boldsymbol{\xi}_{11}\mathbf{u}_1(t)-\boldsymbol{\xi}_{12}\mathbf{u}_2(t)-k\mathbf{r}_1(t)+\mathbf{K}_{R,1}(t),\\ m\frac{d\mathbf{u}_2(t)}{dt}&=-\boldsymbol{\xi}_{11}\mathbf{u}_2(t)-\boldsymbol{\xi}_{12}\mathbf{u}_1(t)-k\mathbf{r}_2(t)+\mathbf{K}_{R,2}(t),\end{aligned} \tag{10}$$

where the random force $\mathbf{K}_{R,i}(t)$ is Gaussian with a vanishingly short correlation time,

$$\langle\mathbf{K}_{R,i}(t)\mathbf{K}_{R,j}(t')\rangle=2k_BT\boldsymbol{\xi}_{ij}\delta_{ij}\delta(t-t'). \tag{11}$$

Because there is no coupling between motion parallel and perpendicular to the separation vector $\mathbf{r}$, we drop the vector notation from here on and consider only the parallel (x) direction. Equation (10) is solved by standard techniques. The dynamics is first decomposed into the two independent modes,

$$\begin{aligned} X_+&=\frac{1}{\sqrt{2}}(x_1+x_2),\\ X_-&=\frac{1}{\sqrt{2}}(x_1-x_2),\end{aligned} \tag{12}$$

which describe, in turn, a cooperative and relative motion of the two spheres. The mean-square displacement of the independent modes, $\langle\Delta X_\pm^2(t)\rangle=\langle[X_\pm(t)-X_\pm(0)]^2\rangle$, may be written formally as

$$\langle\Delta X_\pm^2(t)\rangle=\frac{k_BT}{\pi i}\int_{-i\infty}^{+i\infty}ds\,e^{st}\frac{1}{s^3m+s^2\xi_\pm+sk}, \tag{13}$$

where $\xi_\pm=\xi_{11}\pm\xi_{12}$ and s is the Laplace frequency. The inverse Laplace transform is readily performed to yield

$$\langle\Delta X_\pm^2(t)\rangle=\frac{2k_BT}{k}-\frac{2k_BT}{m(a_\pm-b_\pm)}\left[\frac{1}{b_\pm}e^{-tb_\pm}-\frac{1}{a_\pm}e^{-ta_\pm}\right] \tag{14}$$

with

$$\begin{aligned} a_\pm&=\frac{1}{2m}[\xi_\pm+(\xi_\pm^2-4mk)^{1/2}],\\ b_\pm&=\frac{1}{2m}[\xi_\pm-(\xi_\pm^2-4mk)^{1/2}].\end{aligned} \tag{15}$$

In the strongly overdamped limit, where $\xi_\pm^2\gg4mk$, $\langle\Delta X_\pm^2(t)\rangle$ decays on two widely separated times scales, a fast Brownian scale, $\tau_B=m/\xi_\pm$ and a second slower interaction time scale $\tau_I=\xi_\pm/k$. For typically sized colloids, $\tau_B\sim10^{-7}$ s and so the fast decay is essentially complete on our experimental time scale. For $t\gg\tau_B$, the mean-square displacement is given by the asymptotic expression,

$$\langle\Delta X_\pm^2(t)\rangle_{t\gg\tau_B}=\frac{2k_BT}{k}[1-e^{-kt/\xi_\pm}] \tag{16}$$

and the particle correlation is from Eq. (12),

$$h_{11}(t)_{t\gg\tau_B}=\frac{1}{2}[e^{-kt/\xi_+}+e^{-kt/\xi_-}],$$

$$h_{12}(t)_{t\gg\tau_B}=\frac{1}{2}[e^{-kt/\xi_+}-e^{-kt/\xi_-}]. \tag{17}$$

From these equations, it is clear that the cross correlation $h_{12}(t)$, in particular, is very sensitive to the asymmetry in the relaxation times between the cooperative and relative modes. The cross correlation has a minimum at $t=t_{min}$ that, to leading order in the ratio ξ_{12}/ξ_{11}, is fixed by the individual friction coefficient,

$$t_{\min}=\frac{\xi_{11}}{k}\left[1-\frac{2}{3}\left(\frac{\xi_{12}}{\xi_{11}}\right)^2+\cdots\right], \tag{18}$$

while the depth of the minimum, depends on a ratio of friction coefficients,

$$h_{12}(t_{\min})=e^{-1}\frac{\xi_{12}}{\xi_{11}}\left[1+\frac{1}{6}\left(\frac{\xi_{12}}{\xi_{11}}\right)^2+\cdots\right]. \tag{19}$$

Hence, a fit to $h_{12}(t)$ can yield both friction coefficients. By way of contrast, the autocorrelation function changes only slightly with separation. Indeed, at short times, $h_{11}(t)$ is well approximated by a single exponential $h_{11}(t)\simeq e^{-t/\tau_s}$ with an effective short-time decay time $\tau_s^{-1}=-\lim_{t\to 0} d\ln h_{11}(t)/dt$,

$$\tau_s=\frac{\xi_{11}}{k}\left(1-\frac{\xi_{12}^2}{\xi_{11}^2}\right). \tag{20}$$

For widely separated particles (where $|\xi_{12}|\ll|\xi_{11}|$) τ_s converges to ξ_{11}/k.

IV. RESULTS

The trajectories of a pair of isolated spheres were measured for a number of different center-to-center separations ($2.06\,\mu\text{m}<r<18.87\,\mu\text{m}$). The coordinates of both spheres, parallel and perpendicular to the vector $\mathbf{R}=\mathbf{R}_2-\mathbf{R}_1$ linking the two optical traps, were recorded with a precision of $\approx$1 nm at intervals of 50 μsec for about 8 min in total duration. At each separation, the strengths of the laser traps were determined from a measurement of the Brownian fluctuations of a single trapped particle. The intensities of the two beams were then carefully adjusted until the force constants of the two traps differed by less than $\pm$2%. Each optical trap was essentially isotropic, with force constants measured parallel and perpendicular to $\mathbf{R}$ differing by less than $\sim$7%. While the force constant of the external potential varied somewhat with the exact size of the trapped sphere, measured values were of the order of $5.1\times10^{-6}\,\text{Nm}^{-1}$, for a laser intensity (at the sample) of about 30 mW. The corresponding rms displacement of each trapped sphere is $\approx$40 nm, which is sufficiently small in comparison with typical center-to-center separations to ensure that all dynamical correlations were recorded at an essentially fixed pair separation.

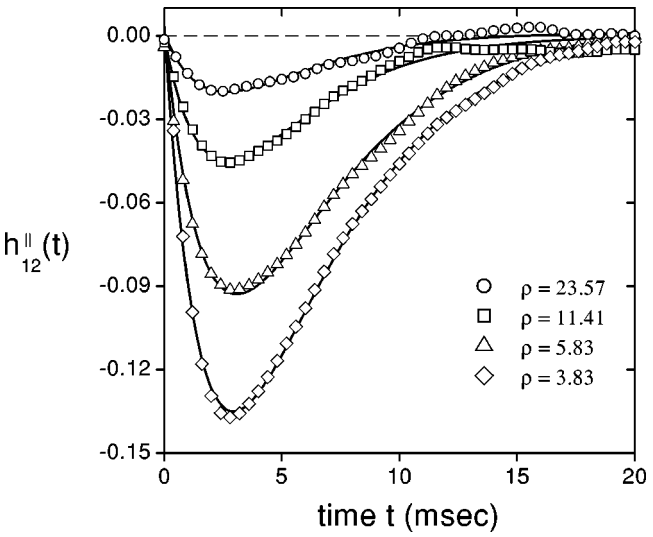

FIG. 4. The time dependence of the correlation $h_{12}(t)$ between the center positions of a pair of spheres, parallel to the separation vector **r**, at four different normalized center-to-center separations. The two 0.652-μm-radius PMMA spheres were held a mean distance r apart by two equal-strength optical traps of force constant $k=5.1\times10^{-6}\,\text{Nm}^{-1}$. The measured cross correlations (indicated by the symbols) were determined from a dataset consisting of 8.4 million measurements of the instantaneous positions of the two spheres at intervals of 50 μs. For clarity, only every tenth measured value is plotted. The solid lines through the data is a fit to Eq. (17).

A typical set of data collected from a pair of 0.652 μm radius spheres at four different center-to-center separations ($\rho=r/\bar{a}$ with $\bar{a}$ the mean particle radius) is shown in Fig. 4; we plot the normalized cross-correlation function $h_{12}(t)$ for motion parallel to the separation vector **R** versus the delay time t. As a result of averaging over 8 million particle pairs, the signal-to-noise ratio of the data is good at short times. At longer times, there are additional random fluctuations that limit the overall signal-to-noise level of our data; these long-time fluctuations are caused mainly by base-line drifts in the detection signals as a result of laser pointing instabilities. The data reveals clearly how the trajectory of one particle is affected by the motion of a neighboring sphere through hydrodynamic interactions. First, the lack of correlation evident in Fig. 4 at very short time scales confirms the absence of any direct potential coupling between the two spheres since the particle trajectories are not *statically* correlated at $t=0$. The stochastic displacements of the two trapped spheres are coupled only by hydrodynamic interactions. Second, the correlations seen in Fig. 4 are entirely *dynamical* in origin; no correlations are present at the longest time scales of our experiment. The coupling seen is a dynamic time-dependent phenomenon that arises as a consequence of particle motion through the surrounding fluid. Finally, we note rather surprisingly that the correlations between particle displacements are antisymmetric (as noted in Ref. [8]) and extremely long ranged (measurable at pair separations $>$30 particle radii).

For a quantitative interpretation of the data, we have fitted the measured cross correlation to the theoretical expression, given in Eq. (17), using the experimentally measured values

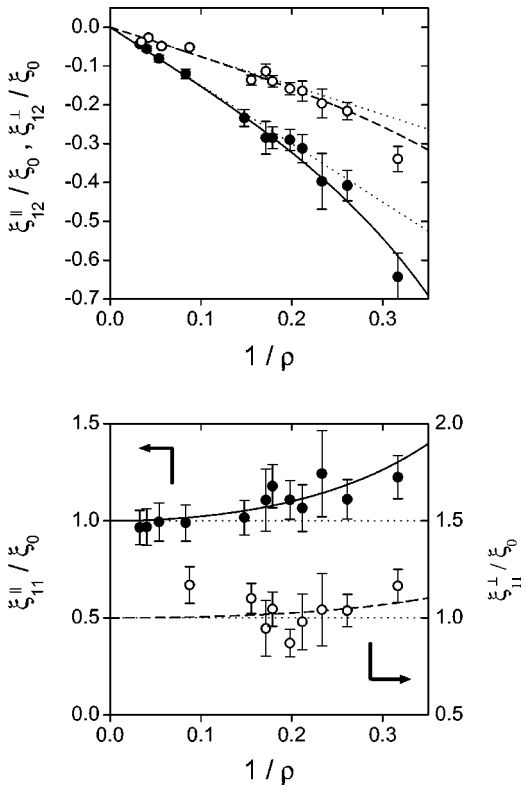

FIG. 5. The joint (top) and self (bottom) friction coefficients measured for a pair of spheres as a function of the inverse dimensionless separation $1/\rho = a/r$. The values are normalized by ξ_0, the friction coefficient of an isolated sphere. The filled circles denote measurements parallel to the pair separation vector **r** and open circles perpendicular to **r**. The solid and dashed curves are the theoretical predictions, calculated with no adjustable parameters from Eqs. (21) and (22), for the parallel and perpendicular geometries, respectively. The data is in excellent agreement with the theoretical low-Reynolds number predictions. The dotted lines indicate the long-range asymptotic behavior.

for the force-constant k. A small sample of the resulting fits are shown by the solid curves in Fig. 4. Agreement is seen as generally very good. From this least-squares fitting procedure, we extract directly the separation dependence of the friction coefficients for the collective $[\xi_{+}^{\parallel}(\rho)]$ and relative motion $[\xi_{-}^{\parallel}(\rho)]$ parallel to the pair separation vector, or equivalently, the self $[\xi_{11}^{\parallel}(\rho)]$ and interaction friction coefficients $[\xi_{12}^{\parallel}(\rho)]$. The resulting values are shown in Fig. 5 plotted versus the inverse particle pair separation $1/\rho$. The same procedure was used to analyze the transverse correlation functions $g_{ij}(t)$ yielding the resulting friction coefficients for motion perpendicular to the interparticle vector **r**, plotted in Fig. 5. It is clear from this figure that the self and interaction friction coefficients exhibit markedly different distance dependencies. While the self-friction coefficient is only weakly dependent on the pair separation, the interaction coefficient, by contrast, varies inversely with the pair separation ρ, at least for large distances. This distance dependence is evident in the data plotted in Fig. 4 where the time of the minimum in the cross correlation (t_{min}) does not change noticeably with separation (from Eq. (18), $t_{\min} \approx \xi_{11}/k$) while the depth of the minimum, which is essentially $\xi_{12}/e\xi_{11}$, is seen to change substantially with ρ.

Our experimental measurements for the distance and geometry dependence of the friction tensor may be compared directly with accurate calculations of the low-Reynolds number hydrodynamic interactions between a pair of identically sized spheres. For the case when the spheres are well separated, Jeffrey and Onishi [17] have given the following asymptotic expressions for the elements of the friction tensor, parallel ($\parallel$) to the interparticle vector **r**,

$$\frac{\xi_{11}^{\parallel}}{\xi_0} = 1 + \frac{9}{4\rho^2} + \frac{93}{16\rho^4} + \frac{1197}{64\rho^6} + \mathcal{O}(\rho^{-8}),$$

$$\frac{\xi_{12}^{\parallel}}{\xi_0} = -\frac{3}{2\rho} - \frac{19}{8\rho^3} - \frac{387}{32\rho^5} + \mathcal{O}(\rho^{-7}), \tag{21}$$

and perpendicular ($\perp$) to **r**,

$$\frac{\xi_{11}^{\perp}}{\xi_0} = 1 + \frac{9}{16\rho^2} + \frac{465}{256\rho^4} + \frac{14745}{4096\rho^6} + \mathcal{O}(\rho^{-8}),$$

$$\frac{\xi_{12}^{\perp}}{\xi_0} = -\frac{3}{4\rho} - \frac{59}{64\rho^3} - \frac{2259}{1024\rho^5} + \mathcal{O}(\rho^{-7}), \tag{22}$$

where $\xi_0 = 6\pi\eta a$ is the friction coefficient of an isolated sphere. The theoretical predictions for the distance dependence of the friction coefficients are shown in Fig. 5 by the solid and dashed curves. The agreement with the experimental data is excellent, particularly when it is recalled that there are no adjustable parameters in the comparison.

While the joint correlation between spheres is clearly affected by their proximity, the effect of hydrodynamic coupling on the individual particle autocorrelations is more subtle. The analysis of Sec. III predicts that the normalized autocorrelation function $h_{11}(t)$ should be a sum of two exponentially decaying terms, a rapid collective mode, and a slower relaxation due to the relative motion of the two spheres. The relaxation times of the two modes are equal if the spheres are well separated and differ significantly from each other only at small separations. Consequently, we expect $h_{11}(t)$ to be a single exponential at large separations and to exhibit an increasing degree of nonexponentiality as the particle separations is progressively reduced. Our data for the correlation function $h_{11}(t)$ for motion parallel to **r**, plotted in Fig. 6, confirms this prediction with significant deviations from an exponential decay evident only at the smallest pair separations. The inset diagram displays the initial decay time τ_s (scaled by the single-particle decay time $\tau_0 = \xi_0/k$), determined from a fit to the parallel autocorrelation data for $t < 1$ msec, as a function of the particle pair separation. The solid curve depicts the theoretical dependence expected from Eqs. (20) and (21). Agreement is again very convincing.

Finally, on first sight, the observation that the measured joint correlation is negative is a little surprising since, as a result of hydrodynamic interaction, one might have expected a particle to tend to move a neighboring particle in the same direction. However, the net fluid flow across any closed

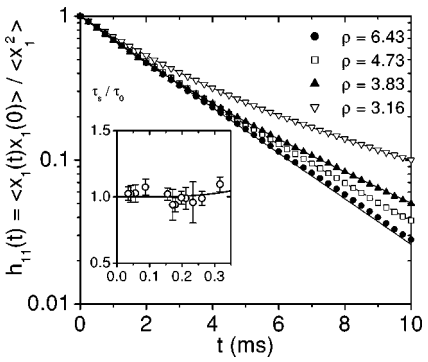

FIG. 6. The single-particle position autocorrelation function $h_{11}(t)$, for displacements parallel to the interparticle vector **r**, measured at four different center-to-center separations ρ. The data is well represented by an exponential at large separations but shows an increasing deviation from a simple exponential decay with reducing particle separation. The inset shows the limiting short-time decay time determined from the measured autocorrelation functions as a function of the inverse pair separation. The values are scaled by the asymptotic limiting decay time τ_0 measured when the particles are widely separated. The solid curve indicates the theoretical predictions of Eqs. (20) and (21).

plane must vanish in an incompressible fluid. Consequently, outside the laminar wake generated by a moving particle there will always be an additional backflow of displaced fluid, directed back towards the moving particle [18]. A neighboring particle swept along by this backflow will tend to become anticorrelated with the original particle. The degree of correlation observed between two spheres depends on the relative proportions of the symmetric (collective) and antisymmetric (relative) modes excited. This ratio is time dependent because hydrodynamic interactions between the two spheres cause the collective mode to relax more rapidly than the relative mode. This is easily confirmed from Eqs. (21) and (22), which provide the following explicit expressions for the collective (ξ_+) and relative (ξ_-) friction constants,

$$\frac{\xi_{\pm}^{\parallel}}{\xi_0} = 1 \mp \frac{3}{2\rho} + \mathcal{O}(\rho^{-2}),$$

$$\frac{\xi_{\pm}^{\perp}}{\xi_0} = 1 \mp \frac{3}{4\rho} + \mathcal{O}(\rho^{-2}), \tag{23}$$

where the upper signs apply to the collective mode and the lower to the relative. The friction coefficients for the collective mode are reduced because of the tendency for the fluid flow generated by one sphere to entrain and sweep along a neighboring sphere. Relative friction coefficients are increased because of the difficulty of squeezing fluid out of or into the gap between two approaching spheres. In consequence, the relative fluctuations generated by the particle pair decay at a slower rate than the collective fluctuations and the particle trajectories develop a pronounced anticorrelation. The observed anticorrelation is however dynamical since on a longer time scale all fluctuations decay and the spheres eventually become uncorrelated.

V. CONCLUSIONS

In this paper, we have shown that hydrodynamic interactions lead to strong long-range correlations between the trajectories of Brownian particles. From an analysis of coupled trajectories we have measured directly the distance dependence of all of the elements of the friction tensor between a pair of particles, both parallel and perpendicular to the pair separation vector. The measured values are in excellent agreement with low-Reynolds number predictions for pairwise hydrodynamics.

ACKNOWLEDGMENTS

We thank Bob Jones, Bob Simmons, Mike Bailes, and Andrew Campbell for useful discussions and comments. This work was supported by the UK Engineering and Physical Sciences Research Council under Grant No. GR/L37533.

[1] P. N. Pusey, in *Liquids, Freezing and Glass Transition*, NATO Advanced Studies Institute, Les Houches, Session LI, 1989, edited by J. P. Hansen, D. Levesque, and J. Zinn-Justin (North-Holland, Amsterdam, 1991), pp. 763–942.
[2] J. Brady and G. Bossis, Annu. Rev. Fluid Mech. **20**, 111 (1988).
[3] H. Tanaka and T. Araki, Phys. Rev. Lett. **85**, 1338 (2000).
[4] M. Smoluchowski, Bull. Int. Acad. Polonaise Sci. Lett. **1A**, 28 (1911).
[5] M. P. Brenner, Phys. Fluids **11**, 754 (1999).
[6] P. J. Mucha, I. Goldhirsch, S. A. Orszag, and M. Vergassola, Phys. Rev. Lett. **83**, 3414 (1999).
[7] D. Riese, G. Wegdam, W. L. Vos, R. Sprik, D. Fenistein, J. Bongaerts, and G. Grubel, Phys. Rev. Lett. **85**, 5460 (2000).
[8] J.-C. Meiners and S. R. Quake, Phys. Rev. Lett. **82**, 2211 (1999).
[9] E. R. Dufresne, T. M. Squires, M. P. Brenner, and D. G. Grier, Phys. Rev. Lett. **85**, 3317 (2000).
[10] B. Lin, J. Yu, and S. A. Rice, Phys. Rev. E **62**, 3909 (2000).
[11] J. C. Crocker, J. Chem. Phys. **106**, 2837 (1997).
[12] L. Antl, J. W. Goodwin, R. D. Hill, R. H. Ottewill, S. M. Owens, S. Papworth, and J. A. Waters, Colloids Surface **17**, 67 (1986).
[13] S. Henderson, S. Mitchell, and P. Bartlett, Colloids Surf., A **190**, 81 (2001).
[14] F. Gittes and C. F. Schmidt, Opt. Lett. **23**, 7 (1998).
[15] G. E. Uhlenbeck and L. S. Ornstein, Phys. Rev. **36**, 823 (1930).
[16] J. Happel and H. Brenner, *Low Reynolds Number Hydrodynamics* (Prentice-Hall, London, 1965).
[17] D. J. Jeffrey and Y. Onishi, J. Fluid Mech. **139**, 261 (1984).
[18] L. Landau and E. Lifshitz, *Fluid Mechanics*, Vol. 6 of *Course of Theoretical Physics*, 2nd ed. (Pergamon, Oxford, 1987).